DOI: 10.1016/j.solener.2011.09.029.

Publication source: Lenert, Andrej, and Evelyn N. Wang. "Optimization of Nanofluid Volumetric Receivers for Solar Thermal Energy Conversion." Solar Energy 86, no. 1, p. 253–265, 2012.

OPTIMIZATION OF NANOFLUID VOLUMETRIC RECEIVERS FOR SOLAR THERMAL ENERGY CONVERSION

Andrej Lenert and Evelyn N. Wang
Device Research Laboratory
Department of Mechanical Engineering
Massachusetts Institute of Technology
Cambridge, MA, USA

Corresponding Author:
Evelyn N. Wang
Department of Mechanical Engineering
Massachusetts Institute of Technology
77 Massachusetts Avenue, 3-461B
Cambridge, MA 02139, USA
Tel: 1 (617) 324-3311
Email: enwang@mit.edu

DOI: 10.1016/j.solener.2011.09.029.
Publication source: Solar Energy 86, no. 1, p. 253–265, 2012.

ABSTRACT

Improvements in solar-to-thermal energy conversion will accelerate the development of efficient concentrated solar power systems. Nanofluid volumetric receivers, where nanoparticles in a liquid medium directly absorb solar radiation, promise increased performance over surface receivers by minimizing temperature differences between the absorber and the fluid, which consequently reduces emissive losses. We present a combined modeling and experimental study to optimize the efficiency of liquid-based solar receivers seeded with carbon-coated absorbing nanoparticles. A one-dimensional transient heat transfer model was developed to investigate the effect of solar concentration, nanofluid height, and optical thickness on receiver performance. Simultaneously, we experimentally investigated a cylindrical nanofluid volumetric receiver, and showed good agreement with the model for varying optical thicknesses of the nanofluid. Based on the model, the efficiency of nanofluid volumetric receivers increases with increasing solar concentration and nanofluid height. The total receiver-side efficiencies are predicted to exceed 35% when nanofluid volumetric receivers are coupled to a power cycle and optimized with respect to the optical thickness and solar exposure time. This work provides insights as to how nanofluids can be best utilized as volumetric receivers in solar applications, such as receivers with integrated storage for beam-down CSP and future high concentration solar thermal energy conversion systems.

Keywords: volumetric receiver, solar, nanofluid, nanoparticle, direct absorption, CSP

DOI: 10.1016/j.solener.2011.09.029.
Publication source: Solar Energy 86, no. 1, p. 253–265, 2012.

1. INTRODUCTION

The use of concentrated sunlight as a thermal energy source for production of electricity promises to be one of the most viable options to replace fossil fuel power plants. However, the peak efficiencies of existing fossil fuel combined cycle power plants exceed 50% (Langston, 2009) while those of concentrated solar power (CSP) plants are below 20% (Pacheco, 2001; Romero *et al.*, 2002). The relatively poor CSP performance is a result of a low solar-to-thermal efficiency (a combination of receiver and field efficiencies) and moderately low operational temperatures in the power cycle. Improving the conversion of incoming solar radiation to thermal energy at high temperatures is essential to improving the overall power conversion efficiency of CSP plants.

Most concentrated solar thermal technologies today use receivers with absorbing surfaces to convert solar energy from its radiative form into thermal energy. These surfaces are typically black or spectrally selective such that high absorptivity in the solar spectrum is coupled with low emissivity in the infrared (Bogaerts and Lampert, 1983). Although surface-based receivers are efficient at solar to thermal conversion, they are not well suited for transferring heat to a carrier fluid. In particular, at high levels of solar concentration, a large temperature difference between the absorber and the fluid arises. The temperature difference leads to significant emissive losses owing to the quartic dependence of thermal re-radiation on the absorber temperature, and correspondingly, a lowering of the overall conversion efficiency of solar energy. Moreover, the material stability of selective surfaces at temperatures above 800 K has not yet been demonstrated (Pitz-Paal and Trevor, 2008). Alternatively, in a volumetric receiver design, concentrated solar radiation is directly absorbed and more uniformly distributed in the surrounding fluid, which decreases the temperature difference between the absorber and the fluid.

Researchers have suggested various configurations for volumetric receiver designs, including: gas-particle suspensions (Bertocchi *et al.*, 2004; Miller and Koenigsdorff, 1991), liquid films (Bohn and Wang, 1988; Caouris *et al.*, 1978), and metal foams (Fend *et al.*, 2004; Pitz-Paal *et al.*, 1997). In this study, we focus on liquid-based volumetric receivers with integrated storage for central receiver CSP systems with beam-down optics (Epstein *et al.*, 1999; Kribus *et al.*, 1998; Yogev *et al.*, 1998); an example configuration was recently described by Slocum *et al.* (2011) where hillside heliostats focus light onto a molten salt volumetric receiver. The potential advantage of such volumetric receivers (VR) compared to ideal selective surface receivers (SS) is illustrated in the representative schematic temperature profiles of Figure 1. The exact temperature profiles will depend on the flow characteristics in the receivers, but for the same mean fluid temperature (T_f) and solar heat flux (CG_s), the temperature profile in the VR (Figure 1a) can be favorable because the temperature associated with emissive loss is lower than that of the mean fluid temperature (by ΔT). This behavior is referred to as "thermal trapping" in solar thermal literature (Arai *et al.*, 1984; Wijeysundera and Thevendran, 1988), but is physically similar to the "greenhouse effect" (Harries, 2000). On the other hand, the unfavorable temperature profile in the SS (Figure 1b) leads to higher emissive losses. Figure 1c highlights the difference in emissive loss (Δe) between an ideal selective surface with an ideal cutoff wavelength equal to 2 μm (purple) and a non-selective volumetric receiver (black) for the case when the mean fluid temperature is equal to 1000 K and ΔT is equal to 250 K. Thus, volumetric receivers, despite being non-selective, can trap thermal energy more effectively and lead to higher receiver efficiencies.

DOI: 10.1016/j.solener.2011.09.029.

Publication source: Solar Energy 86, no. 1, p. 253–265, 2012.

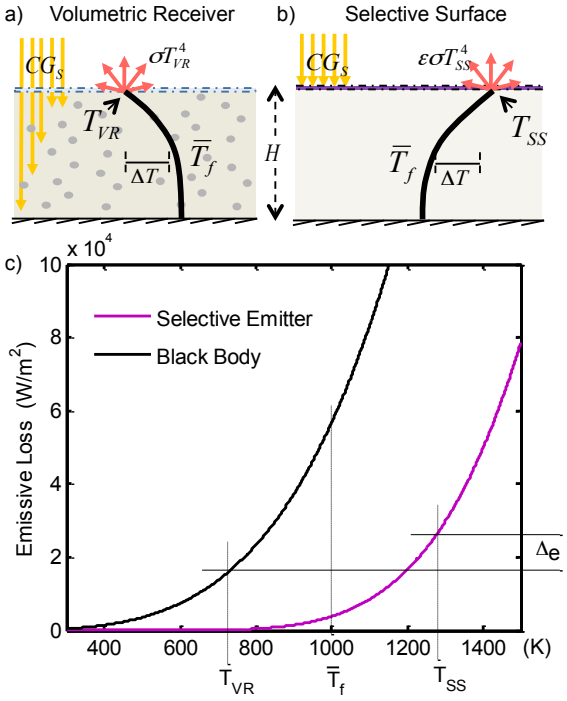

Figure 1. Schematic temperature profiles in a a) non-selective volumetric receiver (VR) compared to a b) surface-based receiver (SS) for the same incoming concentrated solar flux (CG_S) and height (H). The VR has a favorable temperature profile with an inverse ΔT between the mean fluid temperature (T_f) and surface temperature (T_{VR}, T_{SS}). c) The black and purple lines show the emissive loss for a black body (ε=1 at the VR surface) and an ideal selective emitter with a sharp cutoff at 2 μm (ε=ε(T_{ss}) for the SS), respectively. For the case when T_f=1000 K and ΔT=250 K, the emissive loss ($\varepsilon\sigma T^4$) decreases by Δe for the VR.

In particular, volumetric receivers with absorbing small particles in suspension have a high surface-to-volume ratio which minimizes the temperature difference between the absorber and the fluid (Hunt, 1978; Miller and Koenigsdorff, 2000). When the particle size is smaller than the characteristic wavelength of sunlight, less material is required to achieve the same amount of absorption (Hunt, 1978), and challenges related to clogging, sedimentation and erosion can be alleviated.

Past research on small-particle liquid suspensions as VRs has focused on thin liquid films and micro/mini-channel designs. Kumar and Tien (1990) developed a model for particle-laden falling liquid films (1-5 mm thick) incorporating the spectral and directional radiative properties of the particles, and provided a framework for future modeling studies. More recently, Tyagi *et al.* (2009) numerically investigated a low temperature nanofluid receiver inside a mini-channel; while, Otanicar *et al.* (2009b) extended this model to include multiple and dependent scattering, and size-dependent optical properties. Otanicar *et al.* (2010) also experimentally demonstrated the use of different nanofluids in a micro-channel solar collector. However, in these previous studies, the effect of increasing height of the absorbing liquid (H in Figure 1a) beyond the millimeter-scale which can lead to lower emissive loss due to the favorable temperature profile was not considered. Arai *et al.* (1984) investigated transient radiative heating of a static semi-transparent liquid suspension in a taller receiver design (3 cm) and suggested that such a VR

DOI: 10.1016/j.solener.2011.09.029.
Publication source: Solar Energy 86, no. 1, p. 253–265, 2012.

can be highly efficient. Nevertheless, an optimization of small-particle volumetric receivers with respect to particle loading, solar exposure time and nanofluid height has yet to be conducted. As the height of the nanofluid increases, the transient response, representing the thermal charging of these stationary volumetric receivers, becomes a significant portion of the daily operation because of their large thermal inertia.

In this paper, nano-sized (10-100 nm) solid particles are added to a liquid heat transfer fluid (*i.e.,* nanofluid) to volumetrically absorb concentrated solar radiation. We investigate the design of these nanofluid volumetric receivers with nanofluid heights above 1 mm and develop a transient one-dimensional numerical model that examines the effect of solar concentration, nanofluid height, and nanofluid optical thickness on the temperature distribution inside the receiver (Section 2). We studied the effects of varying the optical thickness and validated the numerical model through experiments with a cylindrical nanofluid volumetric receiver, where the radiative and thermophysical properties of the nanofluid were experimentally characterized (Section 3). The model was subsequently used to determine the optimal exposure time and temperature at which point the nanofluid volumetric receiver should be thermally connected to a power generation cycle (Section 4). Throughout this study, a suspension of carbon-coated nanoparticles in Therminol® VP-1 is used as a model system for nanofluid receivers, but the results can also apply to other nanofluid VRs. The outcomes of the work suggest that nanofluids have significant potential as receivers with integrated storage for beam-down CSP systems and future high concentration solar thermal applications.

2. NUMERICAL MODEL

We developed a one-dimensional numerical model to investigate a stationary volumetric receiver undergoing transient heat conduction in the absence of free convection inside the receiver. A schematic of the volumetric receiver concept is shown in Figure 2a. The nanofluid is contained between two parallel plates separated by a variable height (H); the length of the receiver in the horizontal direction is assumed to be large compared to the height. The incident solar heat flux (CG_s), where C represents concentration of solar radiation, is transmitted through the transparent enclosing window and absorbed volumetrically by the suspended nanoparticles. The absorbed radiation results in volumetric heat generation (q_{gen}). The bottom of the receiver is assumed to be adiabatic and specularly-reflective to incident radiation. Radiative heat loss is modeled separately for spectral Band I and II (see Figure 2b). Convective and conductive heat losses are assumed to be negligible in the high temperature regime of interest where radiative loss dominates (Kumar and Tien, 1990).

DOI: 10.1016/j.solener.2011.09.029.

Publication source: Solar Energy 86, no. 1, p. 253–265, 2012.

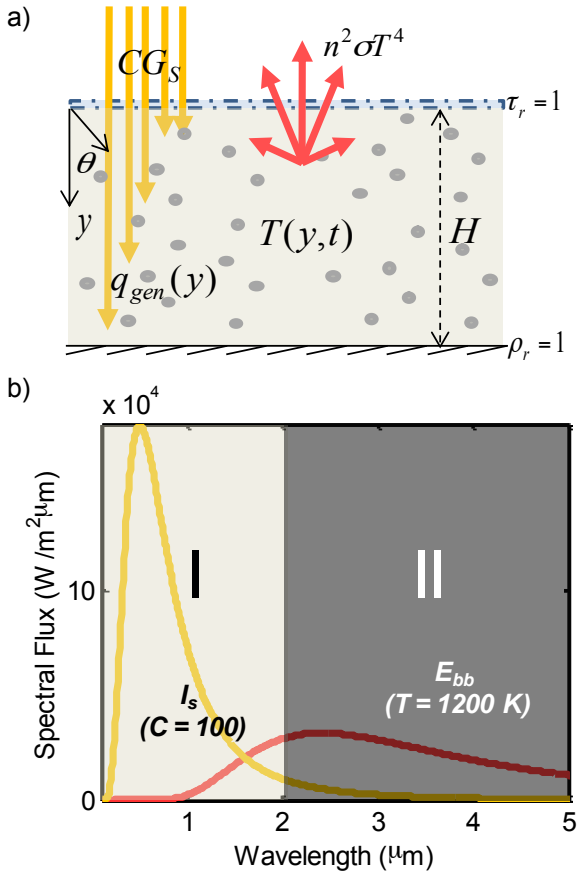

Figure 2. a) Schematic for the model formulation of a 1-D volumetric solar receiver with a transparent top ($y = 0$) where $\tau_r = 1$ and a specularly reflective adiabatic bottom ($y = H$) where $\rho_r = 1$; b) Distribution of concentrated solar irradiation I_S ($C = 100$) and of black body thermal emission E_{bb} at $T = 1200$ K where the radiative properties are separately approximated in two spectral bands, Band I ($\lambda < 2$ μm) and Band II ($\lambda > 2$ μm).

2.1 RADIATIVE PROPERTIES

An ideal carrier fluid would be completely transparent to the incoming solar radiation so that the radiative properties can be tuned *via* the nanoparticles by adjusting their volume fraction. Although they are not currently used as volumetric receivers, high temperature heat transfer fluids in existing solar thermal plants such as Therminol® VP-1 *(Solutia Inc.)* and certain molten salts have solar-weighted absorption below 10% (Drotning, 1978; Otanicar *et al.*, 2009a). For this reason, we assume that the absorptive index (k_f) of the carrier fluid in Band I is much smaller than its refractive index (*i.e.*, $N_f \approx n_f$) in the following treatment.

Suspended nanoparticles with a complex refractive index N_p are utilized to absorb solar radiation in a tunable manner. When the diameter (D) of a nanoparticle is small compared to the wavelength of light inside the medium ($x = \pi D n_f / \lambda << 1$), the nanoparticle has radiative properties which are well-described by the Rayleigh scattering regime (Bohren and Huffman, 1998). This regime also applies for low volume fraction ($f_v << 0.006$) suspensions of polydisperse particles (Brewster and Tien, 1982). If the terms with a higher order of the size parameter are neglected

DOI: 10.1016/j.solener.2011.09.029.
Publication source: Solar Energy 86, no. 1, p. 253–265, 2012.

(since $x << 1$), the particle absorption coefficient ($\kappa_{p,\lambda}$) increases linearly with increasing volume fraction for a given particle material according to:

$$\kappa_{p,\lambda} = \mathrm{Im}\left\{\frac{m^2-1}{m^2+2}\right\}\frac{6\pi f_v}{\lambda} \tag{1}$$

where $m = N_p/n_f$ (Bohren and Huffman, 1998; Modest, 2003). Thus, as long as the overall absorption coefficient of the nanofluid is dominated by the nanoparticles, the optical thickness ($\tau_H = \kappa_\lambda H$) for any given nanofluid height (H) can be tuned by adjusting the volume fraction (f_v) such that most of the solar radiation is absorbed.

For this study, the radiative properties of the nanofluid are approximated using a two-band model. In spectral Band I ($\lambda < 2$ μm in Figure 2b), the nanofluid is approximated as a gray medium ($\kappa_\lambda \approx \kappa_I$) with a tunable optical thickness and a refractive index equal to one ($n_I = 1$). The gray medium simplification is consistent with the experimental results presented in Section 3.1. In spectral Band II ($\lambda > 2$ μm), the nanofluid is modeled as fully absorptive ($\varepsilon_{II} = 1$) because the broad vibrational and rotational absorption bands of the liquid are assumed to overlap and dominate the infrared properties ($\kappa_{II} H >> 1$); this treatment is consistent with previous optical measurements and models of liquids used for direct absorption receivers (Webb and Viskanta, 1985).

2.2 GOVERNING EQUATIONS

To model this physical situation in Figure 2a, the radiative transport and transient heat equation are coupled and solved for a large range of temperatures. The thermophysical properties (k, ρ, c_p) of the nanofluid are assumed to be the same as the bulk fluid based on effective medium theory (Nan *et al.*, 1997) for the low volume fractions considered in this study ($f_v << 0.01$). Moreover, because the high surface-to-volume ratio of the particles leads to instant heat transfer to the surrounding medium (Hunt, 1978; Miller and Koenigsdorff, 2000), the particles and the fluid are assumed to be at the same temperature and the nanofluid is modeled as a single-phase isotropic fluid. To simplify the model further, we assume that the material properties of the nanofluid are independent of temperature. (The validity of this assumption will depend on the choice of carrier fluid; for example, over the working temperature range of VP-1, k, ρ, and c_p do not vary by more than a factor of two).

The radiative transfer equation (RTE) along the y-direction for spectral Band I (see Figure 2) is described by:

$$\mu\frac{dI_\lambda}{dy} = \kappa_I(I_{bb,\lambda} - I_\lambda) \tag{2}$$

where I is the radiative intensity and μ (= cos θ) defines the direction of the propagating radiation with respect to the y-axis (Modest, 2003). The RTE simultaneously describes how the spectral intensity exponentially decays due to absorption and is augmented by thermal re-emission at high temperatures (I_{bb}). The scattering terms are assumed to be negligible because $x << 1$.

Solar radiation is assumed to be normally incident ($\mu = 1$) on the receiver and approximated using Planck's black body distribution ($I_{bb,\lambda}$) at an estimated sun's temperature of 5800 K (T_s); Ω_S is the solid angle of the sun as seen from the Earth (Modest, 2003), and 0.73 accounts for the average attenuation of sunlight through the Earth's

DOI: 10.1016/j.solener.2011.09.029.
Publication source: Solar Energy 86, no. 1, p. 253–265, 2012.

atmosphere such that the nominal solar flux (G_s) is 1000 W/m^2 (1 sun). The top of the receiver is assumed to be transparent ($\tau_r = 1$) to the incident radiation as well as thermal re-emission from inside the receiver, while the bottom of the receiver is assumed to specularly reflective ($\rho_r = 1$); hence, the boundary conditions of the RTE are:

$$I_\lambda(y = 0,\mu) = 0.73\tau_r C\Omega_s I_{bb,\lambda}(T_s)\frac{\delta(\mu - 1)}{2\pi} \qquad 0 \le \mu \le 1 \tag{3-a}$$

$$I_\lambda(y = H,+\mu) = \rho_r I_\lambda(y = H,-\mu) \qquad -1 \le \mu < 0 \tag{3-b}$$

where δ is the Dirac-delta function (Modest, 2003). We couple the RTE to the thermal model through the divergence of the radiative heat flux. The radiative heat flux inside the receiver is determined by integrating the radiative intensity over all of the possible propagation directions and wavelengths in spectral Band I:

$$q_r(y) = 2\pi \int_{\lambda=0}^{2\,\mu m} \int_{\mu=-1}^{1} I_\lambda \mu d\mu d\lambda \tag{4}$$

where the azimuthal component of the solid angle has been integrated to give the 2π pre-factor. Eq. 4 is differentiated with respect to y to obtain the divergence of the radiative heat flux, which is easily incorporated as a volumetric heating term into the heat transfer equation describing unsteady heat conduction:

$$\rho c_p \frac{\partial T}{\partial t} = k\frac{\partial^2 T}{\partial y^2} - \nabla q_r \tag{5}$$

The initial condition and boundary conditions of Eq. 5 are:

$$T(y,0) = T_i \tag{6-a}$$

$$-k\left.\frac{\partial T}{\partial y}\right|_{y=0} = \varepsilon_{II}\left(\sigma T_{amb}^4 - \int_{\lambda=2\,\mu m}^{\infty} \pi I_{bb,\lambda}(T(0,t))d\lambda\right) \tag{6-b}$$

$$\left.\frac{\partial T}{\partial y}\right|_{y=H} = 0 \tag{6-c}$$

We model radiative losses in spectral Band II using the boundary condition at the top of the receiver (Eq. 6-b). For fluid temperatures less than ~800 K, most of the emissive losses are dependent on the fluid properties above 2 μm where it acts as a black body; thus, the surface temperature of the volumetric receiver dominates the amount of heat loss in this regime. At high temperatures, however, thermal re-radiation from within the receiver, captured using the RTE equations, becomes important.

2.3 SOLUTION METHODOLOGY

An analytical solution to Eqs. 2-6 cannot be obtained due to the quartic dependence of radiation on the temperature profile. Instead we solve this set of equations numerically by separating them into two steps. First, we explicitly

DOI: 10.1016/j.solener.2011.09.029.
Publication source: Solar Energy 86, no. 1, p. 253–265, 2012.

solve the RTE equations (Eqs. 2-4) by separating the intensity into the collimated part (*i.e.*, incident radiation) and the diffuse part (*i.e.*, re-emission), and determining the radiative heat flux through numerical integration of Eq. 4 for given a temperature profile at time t_i. Second, the divergence of the radiative heat flux is found by differentiating Eq. 4 with respect to y, which is then incorporated into the energy equations (Eqs. 5-6) to determine the temperature profile at a subsequent time t_{i+1}. This new temperature profile is subsequently re-introduced into the first step, and the two-step procedure is repeated; the methodology is similar to the one described by Kumar and Tien (1990). To solve Eqs. 5-6, a finite difference scheme is used to solve the equations and the boundary conditions along the y-direction, while the 4th order Runge-Kutta method is used to step explicitly in time. A mesh refinement study along the y-direction is performed until the maximum variance in the temperature profile is below 0.01 K. An energy balance is performed for each solution to ensure energy conservation.

2.4 TEMPERATURE PROFILES

Figure 3 shows transient temperature profiles of the nanofluid obtained with the numerical model. In all three cases and throughout this study, typical values for the thermophysical properties of Therminol® VP-1 at room temperature were used (k = 0.1357 W/mK; ρ = 1060 kg/m3; c_p = 1570 J/kgK); for simplicity, they are assumed not to vary with temperature. Although VP-1 begins to break down around 650 K (Moens and Blake, 2008), we extrapolate the material properties of VP-1 to higher temperatures, assuming that molten salts can replace VP-1 as the carrier fluid without significantly altering our model because they have similar radiative properties (Drotning, 1978; Webb and Viskanta, 1985). The initial temperature of the nanofluid is set to room temperature (300 K). With these parameters fixed, the numerical model is used to investigate the effect of solar concentration (C), nanofluid height (H), and optical thickness (τ_H).

DOI: 10.1016/j.solener.2011.09.029.

Publication source: Solar Energy 86, no. 1, p. 253–265, 2012.

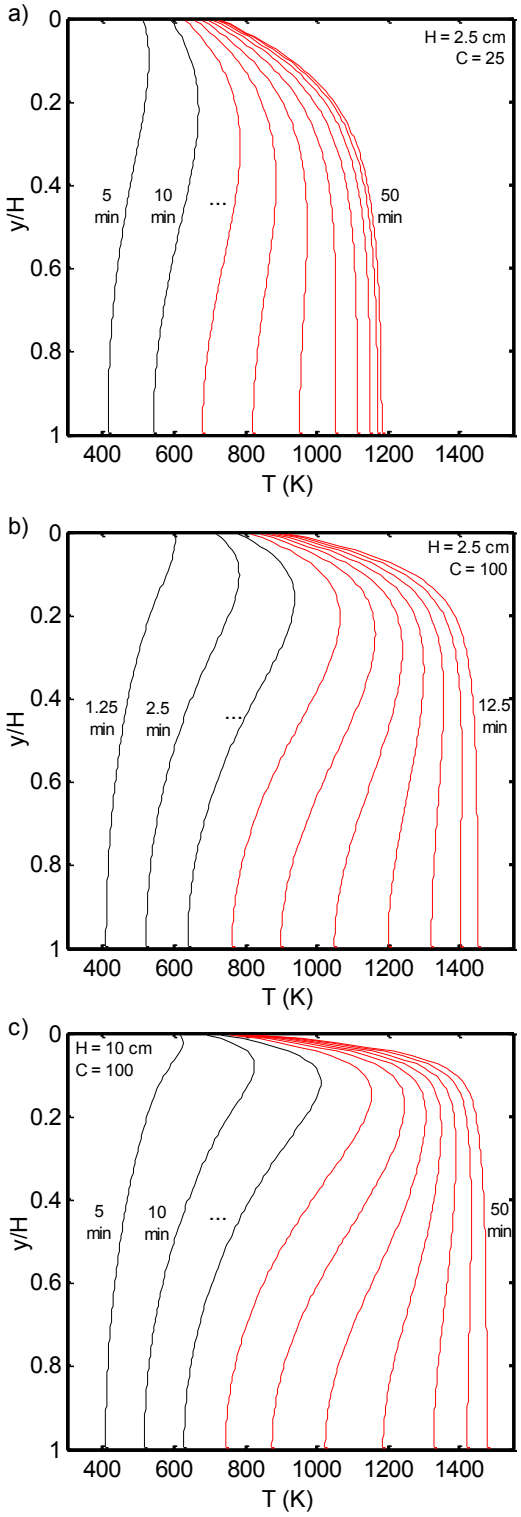

Figure 3. Developing temperature profiles for volumetric receivers from the model with $\tau_H = 1.7$ and varying solar concentrations and nanofluid heights: a) $C = 25$, $H = 2.5$ cm, b) $C = 100$, $H = 2.5$ cm, c) $C = 100$, $H = 10$ cm. The profiles were obtained at regular time intervals: a,c) 5 mins, b) 1.25 mins. The red profiles indicate inverted temperature profiles (*i.e.,* the bulk mean temperature exceeds the top surface temperature)

DOI: 10.1016/j.solener.2011.09.029.
Publication source: Solar Energy 86, no. 1, p. 253–265, 2012.

In this sub-section, we explore the effects of H and C on the developing temperature profiles while maintaining a constant $\tau_H = 1.7$ (the reason for this choice of τ_H will become apparent in Section 4). Figure 3a shows temperature profiles in a 2.5 cm receiver with 25 suns of incident solar radiation ($CG_s = 25$ kW/m^2); in Figure 3b, H remains the same while C is quadrupled ($CG_s = 100$ kW/m^2); and lastly, in Figure 3c, the height is quadrupled ($H = 10$ cm) while C is maintained at 100.

The results in all three cases show that, initially, the temperature at the top of the receiver is higher than the bulk. However, as the temperature profiles develop, the top surface becomes nearly fixed at a temperature while the mean fluid temperature continues to increase leading to inverted temperature profiles (*i.e.,* the bulk mean temperature exceeds the top surface temperature). This temperature profile inversion, characteristic of all three sets of developing profiles, occurs between 600-800 K because the radiative losses from the top surface begin to balance the local solar heat generation in that area, while the rest of the fluid continues to absorb solar radiation and rise in temperature. As temperatures above 1000 K are reached locally in the profile, thermal re-radiation from within the volumetric receiver becomes more important. The radiative mechanism of heat exchange between the relatively hotter and colder spots inside the receiver is more effective than pure conduction, leading to near isothermal profiles at high temperatures in the lower regions of the receiver ($0.2 < y/H < 1$).

A comparison of Figure 3a with 3b shows that increasing the incident solar heat flux (by increasing C) results in increased curvature in the temperature profiles; furthermore, the profiles begin to approach steady state at shorter exposure times and at higher mean temperatures. Similarly, when the nanofluid height is quadrupled (from 3b to 3c), the profile curvature is even more pronounced; however, the exposure time needed to reach the same temperatures as before is inversely proportional to the height. Thus, with increasing C and decreasing H, higher temperatures are achieved in shorter periods of time. This result is intuitive if we approximate the behavior of the nanofluid with a lumped capacitance model.

The numerical results also indicate that the profile inversion is more pronounced for taller receivers. Based on the magnitude of the profile inversion and Figure 1, the results suggest that the receiver efficiency increases with increasing C and H. These effects will be explored further in Section 4, but first, the numerical model is compared to experiments in Section 3.

3. EXPERIMENTAL STUDY

3.1 NANOFLUID PREPARATION AND PROPERTIES

Carbon-coated cobalt nanoparticles *(NanoAmor Inc.)* suspended in Therminol® VP-1 were prepared and studied in this work. C-Co nanoparticles were chosen because graphite has a predictable broadband absorption in the visible and near-IR spectrum. The magnetic (cobalt) core of the nanoparticles could potentially be utilized to control the distribution of the particles inside the receiver; this topic, however, is beyond the scope of this study. Therminol® VP-1 was chosen because of its optical transparency and widespread use in solar thermal power plants.

DOI: 10.1016/j.solener.2011.09.029.

Publication source: Solar Energy 86, no. 1, p. 253–265, 2012.

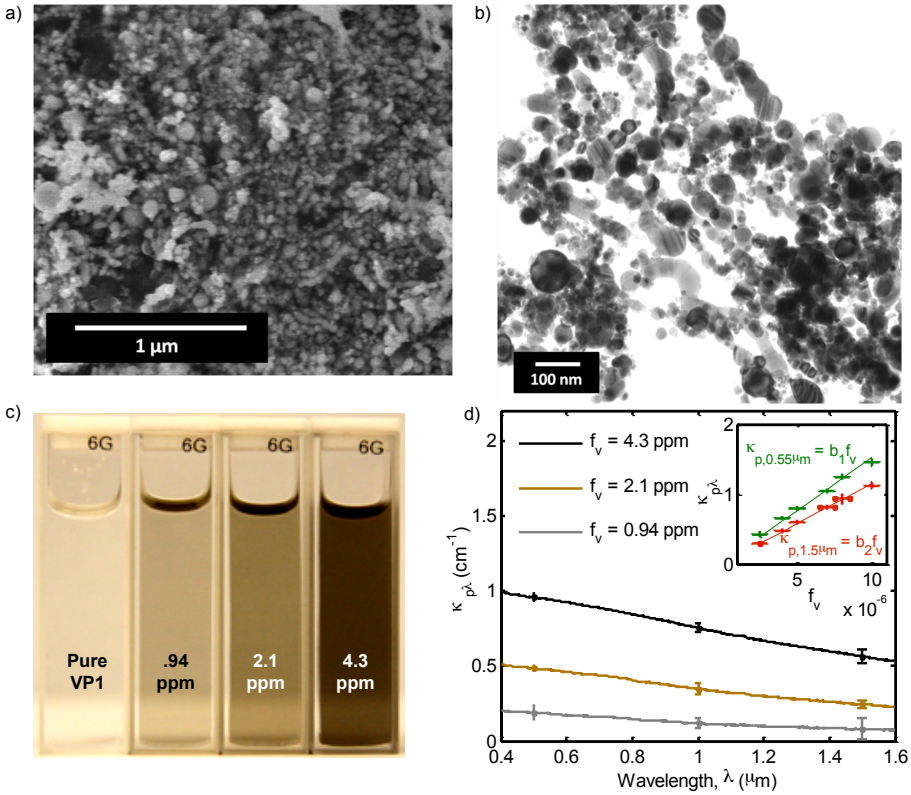

Figure 4. a) Scanning electron micrograph (SEM) and b) Transmission electron micrograph (TEM) of carbon-coated cobalt nanoparticles (NPs) with an average diameter of 28 nm. c) Image of C-Co/VP-1 nanofluid at varying volume fractions (f_v) compared to pure Therminol® VP-1. d) Spectral absorption coefficient ($\kappa_{p,\lambda}$) of NPs in suspension at corresponding volume fractions (f_v). Inset shows the linear dependence of $\kappa_{p,\lambda}$ with f_v for two wavelengths, λ=0.55µm and λ=1.5µm.

Figure 4 shows images of the nanoparticles (NPs) obtained in a high-resolution SEM (Figure 4a) and TEM (Figure 4b). The average diameter of the predominantly spherical nanoparticles is 28 nm according to the manufacturer. The nanoparticles readily dispersed and suspended in Therminol® VP-1 after 30 minutes in a sonicating bath. The suspensions did not require any surfactant to achieve stability exceeding several days.

To determine the radiative properties of the nanoparticles, a differential measurement technique was performed using a spectrophotometer (*Cary 500i*, *Varian Inc.)*. For this measurement, cuvettes of equal pathlengths (10 mm) were used, and the difference in transmission between a sample of nanofluid and a reference of pure VP-1 was determined. The measurement technique is similar to the one recently described by (Sani *et al.*, 2010). The effects of scattering and multiple reflections through media of different optical thickness are assumed to be negligible.

Suspensions of the carbon-coated NPs in VP-1 (C-Co/VP-1) with varying volume fractions were prepared, ranging from 2.5 ppm (f_v = 2.5E-6) to 10 ppm (f_v = 10E-6). The experimental results for the spectral absorption coefficient at three different volume fractions are plotted in Figure 4d showing a slight decay in absorption over the range of wavelengths and a general increase in absorption coefficient with increasing f_v. Since the resulting volumetric heat generation is obtained through an integration over the wavelength range of incident solar radiation

DOI: 10.1016/j.solener.2011.09.029.
Publication source: Solar Energy 86, no. 1, p. 253–265, 2012.

and the absorption characteristics of the C-Co NPs in suspension are not a strong function of wavelength over this range, a solar-weighted absorption coefficient can be used to approximate the resulting volumetric heat generation. This approximation agrees well with the two-band model suggested in Section 2.1. A line of best fit was determined relating each spectral absorption coefficient to the volume fraction, as shown in the inset of Figure 4d for two particular wavelengths. The experimentally determined linear relationship between f_v and $\kappa_{p,\lambda}$ agrees with Eq. 1 and the simplifications made in Section 2.1. The absorption coefficient of Therminol® VP-1 ($\kappa_{f,\lambda}$) was deduced from measurements taken by Otanicar *et al.* (2009a). Using the experimentally determined slope of best fit at each wavelength (b_λ), the effective absorption coefficient of the nanofluid (κ_λ) is predicted as a function of the volume fraction according to Eq. 7.

$$\kappa_\lambda = \kappa_{f,\lambda} + b_\lambda f_v \tag{7}$$

To determine the volume fraction needed for a particular optical thickness (τ_H), a simple iterative algorithm using the semi-empirical approach described above was used in this study. For example, for the 6 cm tall receiver studied in Section 3.2 and the spectrum illustrated in Figure 5b, the corresponding volume fraction is 4.3 ppm for $\tau_H = 4$. A relatively high volume fraction suspension was initially prepared (f_v = 0.001); then, it was diluted in multiple steps with VP-1 to obtain the needed volume fraction.

Table 1. Thermophysical properties of C-Co/VP-1 nanofluid at varying volume fractions (f_v)

Target Opt. Thick. (τ_H)	f_v (ppm)	k (mW/mK) *	c_p (kJ/kgK) **
Pure Therminol® VP-1	0	144.2 +/- 1.4	1.68 +/- .03
1	0.94 +/- .1	145.2 +/- 0.7	1.70 +/- .01
2	2.1 +/-.1	145.1 +/- 0.8	1.67 +/- .03
4	4.3 +/-.1	145.0 +/- 0.7	1.67 +/- .03

* at 30 +/- 5 ^{o}C, measured using Hot Wire Method

** at 31 +/- 1 ^{o}C, measured using a differential scanning calorimeter (*DSC823 Polymer DSC*, *Mettler-Toledo*)

Table 1 shows the volume fractions needed to achieve several optical thicknesses of the C-Co/ VP-1 nanofluid, as well as their corresponding experimentally determined thermophysical properties. The thermal conductivity (k) of the nanofluids was obtained using the Hot Wire Method (Healy *et al.*, 1976), whereas, the ASTM standard test method (*E1269-05*) was followed to obtain specific heat (c_p) using a differential scanning calorimeter (*Polymer DSC823, Mettler-Toledo*). Within the experimental uncertainty, the data suggests that the thermophysical properties are not significantly affected by the addition of NPs, as expected for such low volume fractions.

3.2 EXPERIMENTAL SETUP

The goal of this experimental study was not to replicate the environmental conditions and solar concentration levels that would be typical of a central-receiver design in the field, but to experimentally demonstrate the concept of a

DOI: 10.1016/j.solener.2011.09.029.
Publication source: Solar Energy 86, no. 1, p. 253–265, 2012.

nanofluid volumetric receiver, study the effect of optical thickness and compare the results to the numerical model developed in Section 2. Figure 5a and c show the main components of the setup, including the solar simulator, beam-down mirror, volumetric receiver, thermocouple array and data acquisition system.

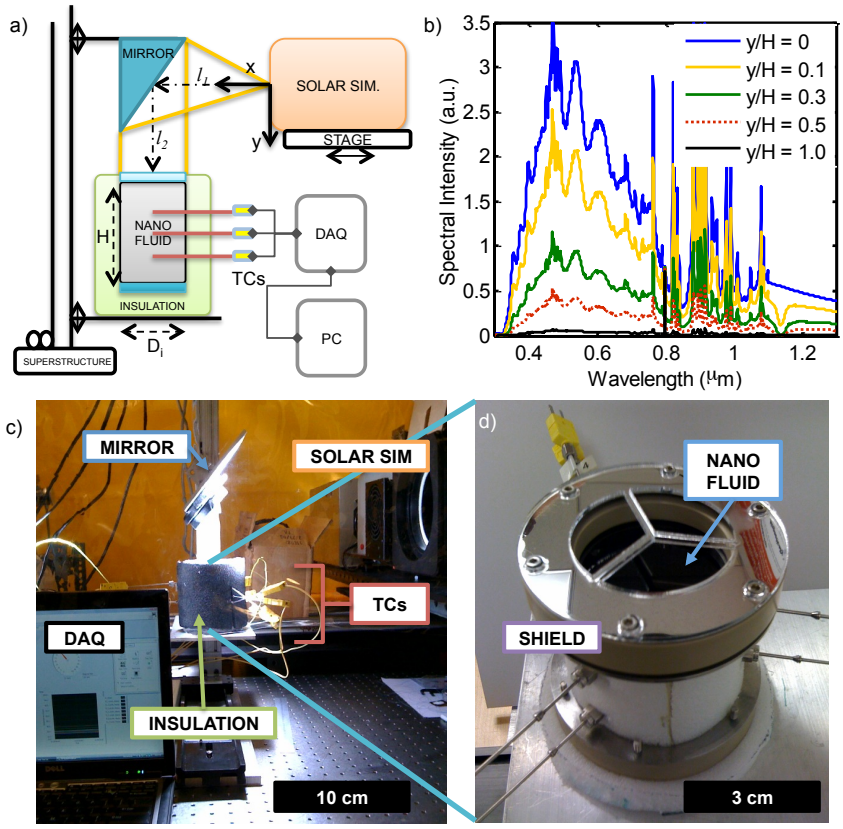

Figure 5. a) Schematic of the experimental setup including a solar simulator (SIM), beam-down mirror, nanofluid receiver, thermocouples (TCs), and data acquisition system (DAQ). b) Spectral intensity of the solar simulator with predicted attenuation along the y-direction of the nanofluid volumetric receiver for $\tau_H = 4$. Image of c) experimental setup with d) volumetric receiver containing C-Co/VP-1 nanofluid.

A 1.6 kW solar simulator *(SS 1600W Fully Reflective, Sciencetech Inc.)* was used as the radiative source for the experiments. The spectral power output of the solar simulator is shown in Figure 5b, as well as the spectral attenuation due to absorption along a receiver with $\tau_H = 4$. The solar simulator matches with the AM1.5 spectrum well and meets ASTM Class A standards for spectral match, temporal stability and spatial uniformity. Before the experiments, the average radiative heat flux incident on the receiver was measured with a power meter and thermopile detector *(1918-C and 818p, Newport Optical)* to be 2460 ± 163 W/m^2.

A custom thin-walled cylinder was machined to hold the nanofluid, shown in Figure 5d. The chamber was fabricated using stainless steel because of its relatively low thermal conductivity (15 W/mK) considering its high structural rigidity and high temperature stability. The chamber was insulated using low-density foam.

Two flanges were used to secure the interchangeable optics to the top and bottom of the cylinder and seal the nanofluid inside. A high-purity quartz window (*1357T33, McMaster*) sealed the top of the cylinder; while the bottom surface was sealed using an enhanced aluminum mirror (*NT46-616, Edmund Optics*), acting as a reflector.

DOI: 10.1016/j.solener.2011.09.029.
Publication source: Solar Energy 86, no. 1, p. 253–265, 2012.

The solar simulator weighted transmissivity (0.926) of the quartz window was measured using a spectrophotometer (*Cary 5E, Varian Inc*.). During the experiments, the radiation from the solar simulator was beamed down to the receiver using an enhanced aluminum mirror (*NT32-666, Edmund Optics*); a laser-cut piece of reflective plastic was used to shield the thermocouples from direct radiation in order to more accurately measure the surrounding fluid temperature.

Temperature measurements were taken using type-K thermocouple probes (*KMQXL-062G-6, Omega*); the probes extended to the centerline of the receiver and were spaced 1 cm apart along the height of the receiver. Seven temperature measurements along the 6 cm height were measured simultaneously for 12 minutes, beginning at the instant the simulated solar radiation reached the receiver.

A data acquisition system was used to record the temperature of each thermocouple averaged over one second. The thermocouple probes were calibrated using a temperature-controlled bath with 0.05 K resolution (*RE-207, Lauda-Brinkmann*). Measurements of temperature close to the wall of the chamber were typically 1-2 K lower than at the centerline, but the vertical profile was determined to be a weak function of the radial distance away from the centerline.

3.3 RESULTS AND COMPARISON WITH NUMERICAL MODEL

Figure 6a, b, and c show experimentally obtained developing temperatures profiles at increments of 100 seconds (triangular symbols) for C-Co/VP-1 nanofluids studied in the test chamber described above with target optical thicknesses of 1, 2 and 4, respectively; the total uncertainty in the temperature measurements is ± 1.7 K for 6a, ± 0.6 K for 6b and ± 0.7 K for 6c. To predict the heat generation profiles (Figure 6 insets), Equation 2 was solved numerically in the cold medium limit (Modest, 2003) using the experimentally determined absorption coefficients (Figure 4d) and the solar simulator spectrum (Figure 5b).

DOI: 10.1016/j.solener.2011.09.029.

Publication source: Solar Energy 86, no. 1, p. 253–265, 2012.

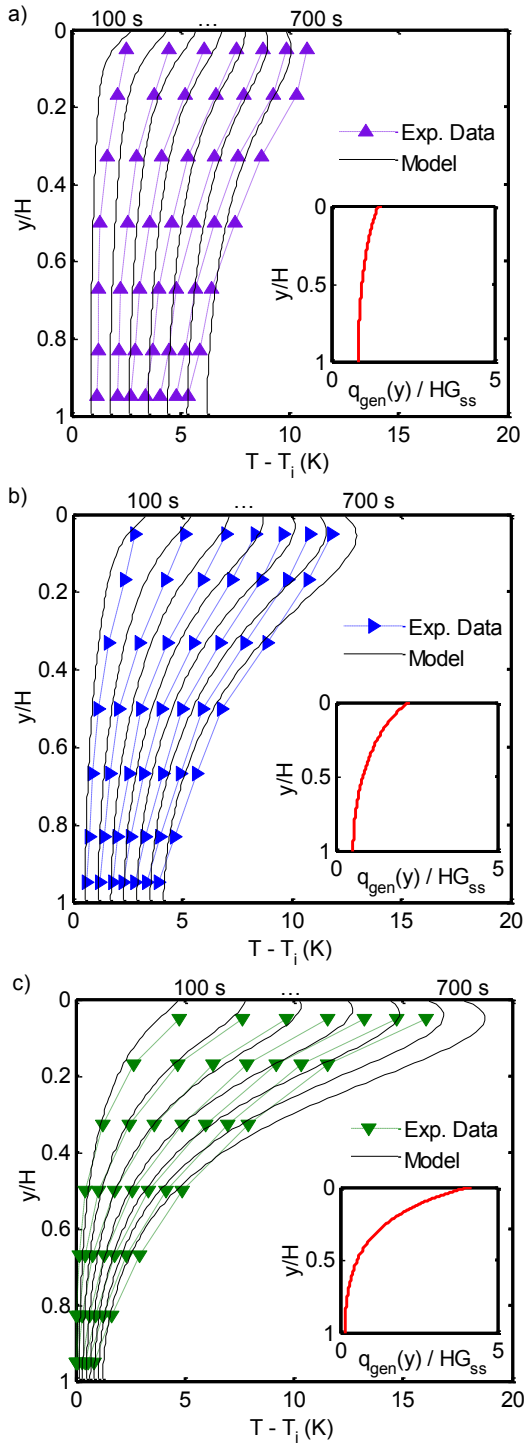

Figure 6. Comparison of the experimentally obtained temperature profiles with numerical results at 100 s intervals for receivers of varying optical thickness: a) $\tau_H = 1$, b) $\tau_H = 2$, c) $\tau_H = 4$. Insets show predicted heat generation profiles based on radiative properties from Figure 4d and solar simulator spectra from Figure 5b.

DOI: 10.1016/j.solener.2011.09.029.
Publication source: Solar Energy 86, no. 1, p. 253–265, 2012.

For all three cases, the shape and decaying nature of the heat generation profile is reflected in the shape of the temperature profiles. With increasing optical thickness, the heat generation profile is increasingly localized to the top of receiver where most of the losses occur.

The numerically predicted temperature profiles (black lines) are shown for the same time increments as the experimental data. To predict these profiles, the numerical model (described in Section 2) was solved using the solar simulator spectrum as the input radiation and the experimental thermophysical properties and absorption coefficients. A convective heat loss coefficient from the top surface (h_{NC} = 5 W/m^{2}K) was calculated analytically and added because the experiments were conducted at temperatures below 350 K where the relative importance of natural convection cannot be neglected as compared to radiative loss. Also, because of the transient nature of the experiment and the comparable vertical (H = 6 cm) and horizontal lengths (6.35 cm inner diameter) of the receiver, our 1-D numerical model was modified for comparison with the experimental results. By design, the walls and optics directly in contact with the nanofluid are thin enough (Bi << 1/6) to be approximated as being at the same temperature as the fluid. Based on a measured weight and heat capacity, the total heat capacitance of the walls is 222 J/K, while that of the nanofluid is 288 J/K. Thus, a significant portion of the thermal energy is stored in the sidewalls. Using a lumped capacitance model, we estimated that 56.5 % of the incident energy results in heating the nanofluid, while the rest of the energy is stored in the sidewalls. By incorporating this scaling factor (which can be estimated *a priori*), the model and experimental results show good agreement. These types of application-dependent improvements on the basic model from Section 2 can be obtained and implemented.

The main discrepancy between the model and experimental results is evident in the temperature profiles near the top surface for τ_H = 4 (6c); the experimental results show a smaller temperature gradient than that of the model prediction. We attribute the discrepancy to the relatively large difference in temperature between the top and the bottom of the receiver which induces a re-distribution of heat *via* the conductive side-walls; this conjugate heat transfer is not captured in our model. In general, the good agreement between the model and experiment (within a 20% difference) suggests that the developed model can be used to investigate volumetric receiver efficiency.

4. RECEIVER OPTIMIZATION

In this section, the volumetric receiver design is optimized on the basis of two important metrics for solar thermal applications: receiver efficiency (η_{rec}), and receiver-side net system efficiency (η_{sys}). The efficiency of a solar thermal receiver is the ratio of collected thermal energy to the total incident energy (Tyagi *et al.*, 2009):

$$\eta_{rec} = \frac{\text{Thermal Energy Stored}}{\text{Incident Solar Energy}} = \frac{mc_p(\overline{T}_f - T_i)}{CG_s A_{rec} t_{\exp}} \tag{8}$$

The metric in the above form applies to stationary receivers undergoing transient heating, where m is the mass of the nanofluid, t_{exp} is the total amount of time exposed to solar radiation and A_{rec} is the top surface area of the receiver.

However, the aim of a solar thermal receiver is not only to convert concentrated solar radiation into thermal energy as efficiently as possible, but also, to achieve the highest possible temperatures while retaining this high

DOI: 10.1016/j.solener.2011.09.029.
Publication source: Solar Energy 86, no. 1, p. 253–265, 2012.

efficiency. The reason to achieve high fluid temperatures becomes evident when a power conversion cycle is placed in series with the solar thermal receiver. Thermal coupling of a stationary volumetric receiver with integrated storage to a power generation system can potentially be achieved through heat exchange with the walls of the nanofluid volumetric chamber or utilizing a flow heat exchanger and a separate cold-storage tank. For simplicity, we assume that this coupling can be accomplished such that there is minimal effect on receiver efficiency. A logical choice to quantify this increase in power conversion efficiency with increasing final mean fluid temperature is the Carnot efficiency:

$$\eta_c = 1 - \frac{T_{amb}}{\overline{T}_f} \tag{9}$$

The total receiver-side efficiency of the solar thermal power generation system becomes:

$$\eta_{sys} = \eta_{rec}\eta_c\eta_{II} \tag{10}$$

which incorporates a constant second-law efficiency (η_{II}) to account for irreversibilities of the power generation cycle, which we assume to be $\eta_{II} = 0.66$ (Singh *et al.*, 2000).

The opposing trends of the receiver efficiency and the Carnot efficiency with increasing temperature give rise to an optimum system efficiency (η_{sys}^{opt}) (Pitz-Paal and Trevor, 2008). We study the effects of the following parameters on the receiver and system efficiency: concentration (C), nanofluid height (H), and optical thickness (τ_H).

Effect of optical thickness: Figure 7a shows the effect of optical thickness on the receiver efficiency (Eq. 8). As discussed previously, the optical thickness of a nanofluid volumetric receiver can be adjusted by varying the volume fraction of the nanoparticles. With increasing optical thickness, volumetric absorption will more closely resemble surface absorption because the photon penetration depth will decrease. With shorter penetration depths, the heat release is localized to the top of the receiver where most of the losses occur; hence, a volumetric receiver with $\tau_H = 4$ is less efficient than one with $\tau_H = 1.7$. On the other hand, if the optical thickness is too small (as is the case when $\tau_H = 1$), the receiver is unable to absorb all of the incident solar radiation. Using the maximum system efficiency as a metric (η_{sys}^{opt}), the optimum optical thickness was determined to be 1.7 (± 0.1), as shown in the inset of Figure 7a. The optical thickness was fixed to this optimum value for the remainder of the study.

DOI: 10.1016/j.solener.2011.09.029.

Publication source: Solar Energy 86, no. 1, p. 253–265, 2012.

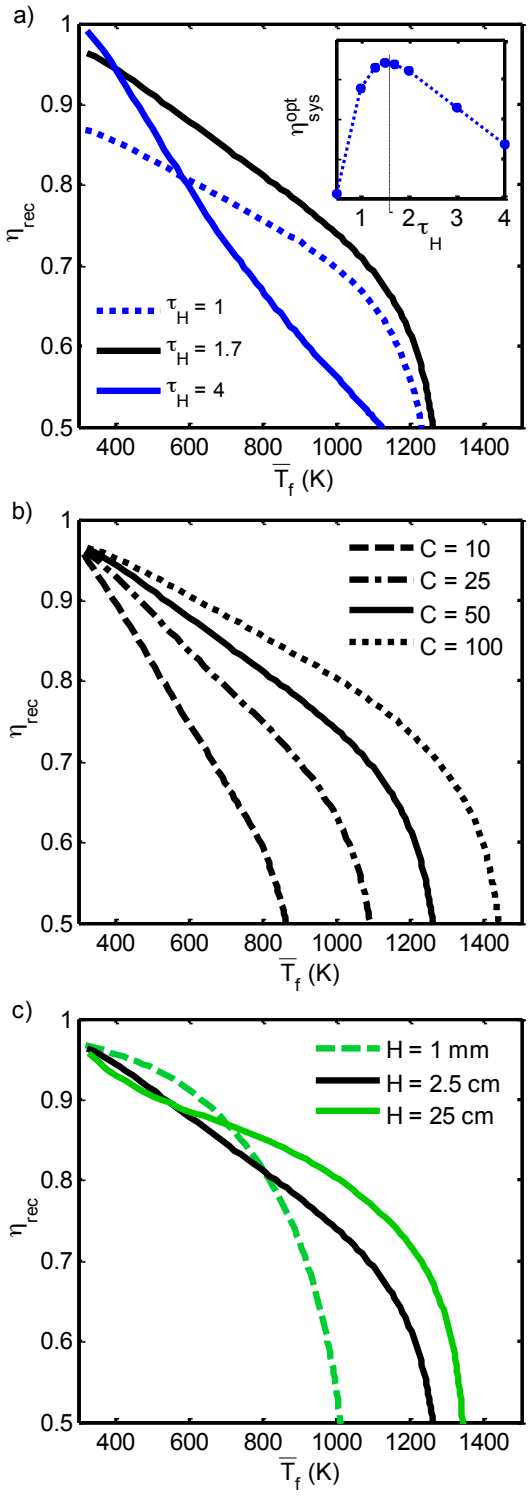

Figure 7. Parametric study of receiver efficiency with mean fluid temperature for variable optical thickness, solar concentration, and nanofluid height: a) τ_H ranging from 0.5 to 4. Inset shows system efficiency with varying optical thickness with the optimum at $\tau_H = 1.7$. b) C ranging from 10 to 100, and c) H ranging from 0.1 to 25 cm. The baseline in all of the graphs (solid black) shows the case when $\tau_H = 1.7$, $C = 50$, and $H = 2.5$ cm.

DOI: 10.1016/j.solener.2011.09.029.
Publication source: Solar Energy 86, no. 1, p. 253–265, 2012.

Effect of solar concentration:

Increasing the concentration (C) of solar radiation incident on a volumetric receiver has the effect of increasing the steady state or stagnation temperature. Higher concentration levels allow the receiver to maintain a high efficiency over a wider range of temperatures and delay the sharp decrease in efficiency as the receiver asymptotes to its stagnation temperature, as seen in Figure 7b. Therefore, receiver efficiency increases with C for the range considered.

A surface plot showing optimum system efficiency in the parameter space of C and H for a nanofluid volumetric receiver with $\tau_H = 1.7$ coupled to an idealized power cycle is shown in Figure 8a. The results show that the optimum system efficiency increases with concentration level.

Effect of nanofluid height:

When the emissive loss is dominated by the top surface temperature, the effect of nanofluid height may be understood by considering that increasing H will amplify the temperature difference between the mean fluid temperature and the surface temperature (as shown in Figure 3). Figure 7c shows how η_{rec} decreases with increasing nanofluid height for temperatures below 700 K, which corresponds to a region where the surface temperature is higher than the mean fluid temperature. For higher temperatures (800-1200 K), η_{rec} increases with increasing nanofluid height because the profile inversion has occurred. At very high temperatures (above 1300 K), H has no effect on receiver efficiency because the dominant volumetric losses (spectral Band I) are only affected by the optical thickness, since they are governed by the RTE (Eq. 2).

In the temperature range where net system efficiency is maximized (800-1200 K), taller nanofluid VRs achieve improved receiver efficiencies because of the profile inversion. Thus, the optimum system efficiency of nanofluid volumetric receiver increases as the volume (*i.e.*, nanofluid height) is increased, as shown in Figure 8a. An upper limit on the nanofluid height is determined by the optical clarity of the carrier fluid since the radiative properties and the optical thickness of the nanofluid need to be dominated by the nanoparticles for this analysis to be valid.

Optimal exposure time and temperature:

With the efficiency of the nanofluid volumetric receiver optimized with respect to optical thickness, we investigate the effects of concentration and nanofluid height on the exposure time and temperature at the optimum system efficiency. Each η_{sys}^{opt} determined in Figure 8a corresponds to a specific final mean temperature (Figure 8b) and exposure time (Figure 8c).

The optimal final mean temperatures are shown in Figure 8b. The trends for optimal temperature follow very closely the trends for optimum system efficiency (Figure 8a) because the system efficiency is strongly dependent on the temperature due to the power cycle efficiency. This analysis shows that nanofluid volumetric receivers need to be stable at very high temperatures in order to reach the predicted optimum system efficiencies. In future work, the material durability at such high temperature needs to be addressed.

DOI: 10.1016/j.solener.2011.09.029.

Publication source: Solar Energy 86, no. 1, p. 253–265, 2012.

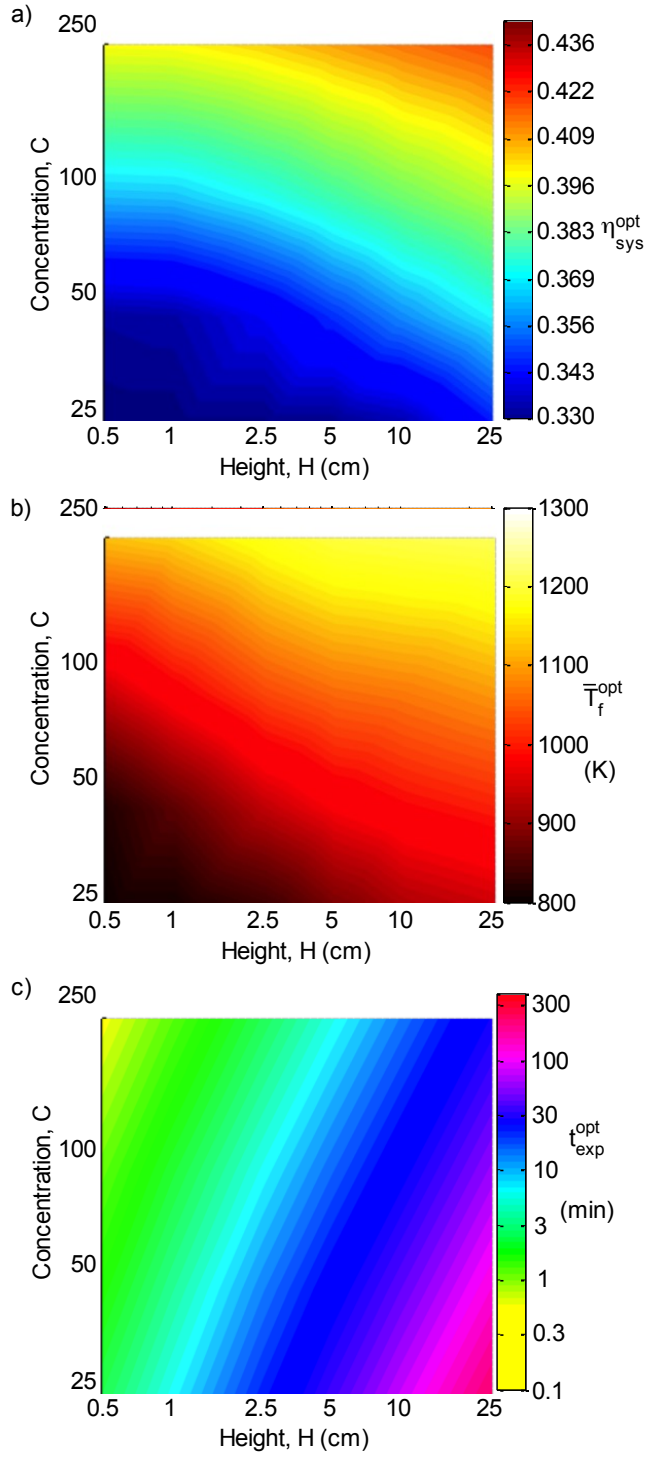

Figure 8. Surface plots showing: a) optimum system efficiency in the parameter space of C and H for nanofluid VRs ($\tau_H = 1.7$), b) optimal final mean temperature, and c) optimal exposure time corresponding to the optimum system efficiency in (a).

DOI: 10.1016/j.solener.2011.09.029.
Publication source: Solar Energy 86, no. 1, p. 253–265, 2012.

As shown in Figure 8c, the amount of exposure time (t_{exp}) needed to achieve optimum system efficiency decreases with increasing concentration and decreasing nanofluid height for nanofluid VRs with $\tau_H = 1.7$. Exposure time is an important quantity in solar thermal plants because a shorter exposure time translates to the capability to store more thermal energy for a limited amount of hours of sunlight.

The results indicate that volumetric receivers are advantageous for applications with high levels of solar concentration such as central receiver designs. Furthermore, because of the increasing efficiency with nanofluid height, nanofluid VRs are well-suited for ground-based liquid receiver tanks with integrated storage where a "reflective tower" (Epstein *et al.*, 1999) or hillside mounted heliostats (Slocum *et al.*, 2011) are used to beam down concentrated solar radiation.

This study provides an important starting point for system-level studies that can extend this analysis to more specific applications by incorporating non-idealities associated with optical concentration, pumping, and storage. As shown in Figure 8a, nanofluid VRs can achieve high ideal system efficiencies exceeding 35% in the parametric space considered.

5. CONCLUSIONS

Nanofluid volumetric receivers for high solar flux and high temperature solar thermal applications were investigated. A 1-D numerical model was developed to predict temperature profiles based on direct absorption by the nanoparticles and thermal re-emission at high temperatures. The radiative properties of the nanofluid were tuned by adjusting the particle loading to achieve a desired optical thickness. An experimental setup was used to measure temperature profiles in suspensions of 28 nm carbon-coated cobalt nanoparticles in Therminol® VP-1 for varying nanofluid optical thicknesses; the experimental results are in good agreement with the numerical modeling results (within a 20% difference). The model shows that receiver efficiency increases with increasing nanofluid height and incident solar flux, and that the optimum optical thickness for a non-selective volumetric receiver is 1.7 ± 0.1. When connected to a power cycle, optimum system efficiencies exceeding 35 % are predicted when $C > 100$ and $H > 5$ cm. The outcomes of the study provide an important perspective as to how nanofluids can be best utilized as volumetric receivers in concentrated solar applications.

NOMENCLATURE

A	Total surface area exposed to solar radiation [m^2]
b	Slope of best fit between $\kappa_{p,\lambda}$ and f_v [m^{-1}]
Bi	Biot number
C	Solar concentration factor [-]
c_p	Heat capacity [J/kg-K]
D	Particle diameter [m]
e	Emissive power [W/m^2]
E_{bb}	Black body emission [W/m^2-m]
f_v	Particle volume fraction [-]
G	Incident radiative heat flux [W/m^2]
H	Nanofluid height [m]
I	Radiative intensity [W/m^2-m-sr]

DOI: 10.1016/j.solener.2011.09.029.

Publication source: Solar Energy 86, no. 1, p. 253–265, 2012.

k Thermal conductivity [W/m-K] / Absorptive index [-]
m Relative refractive index (N_p/n_f) [-] / Mass of the nanofluid [kg]
n Refractive index [-]
N Complex refractive index of a medium ($n + ik$) [-]
q Heat flux [W/ m^2]
q_{gen} Heat generation inside receiver [W/ m^3]
Ω_s Solid angle of sun as seen from Earth = 6.80 (10^{-5}) sr
T Temperature [K]
t Time [s]
x Size parameter: $\pi D n_f/\lambda$ [-]
y Coordinate [m]

Greek Symbols
δ Dirac-delta function
ε Emissivity [-]
η Efficiency [-]
θ Polar angle inside volumetric receiver [rad]
κ Absorption coefficient [m^{-1}]
λ Wavelength of light in vacuum [m]
μ Directional cosine w.r.t. to y-axis ($\cos\theta$) [-]
ρ Density [kg/m^3]
ρ_r Specular reflectivity [-]
σ Stefan-Boltzmann constant = 5.670 (10^{-8}) W/m^2-K^4
τ_H Optical thickness [-]
τ_r Transmissivity [-]

Superscript
$\bar{}$ Mean or average value
opt Optimum value

Subscripts
I for $\lambda < 2\mu m$
II for $\lambda > 2\mu m$
bb Black body
exp Exposure to solar radiation
f Fluid medium
i Initial (t = 0)
λ Spectral
p Particle
rec Receiver
r Radiative
s Solar / solar simulator
SS Ideal selective surface-based receiver
VR Volumetric receiver

ACKNOWLEDGEMENTS

The authors would like to thank the King Fahd University of Petroleum and Minerals in Dhahran, Saudi Arabia, for partially funding the research reported in this paper through the Center for Clean Water and Clean Energy at MIT and KFUPM. Also, Andrej Lenert acknowledges the support of the MIT Energy Initiative and the National Science Foundation Graduate Fellowship. We sincerely thank: Daniel Kraemer and Jianjian Wang for their experimental help, Mattheus Ueckermann for his numerical advice, and members of the CSPonD project at MIT for the insightful discussions.

DOI: 10.1016/j.solener.2011.09.029.

Publication source: Solar Energy 86, no. 1, p. 253–265, 2012.

REFERENCES

Arai, N., Itaya, Y., Hasatani, M., 1984. Development of a volume heat-trap type solar collector using a fine-particle semitransparent liquid suspension (FPSS) as a heat vehicle and heat-storage medium. Sol. Energy. 32, 49-56.

Bertocchi, R., Karni, J., Kribus, A., 2004. Experimental evaluation of a non-isothermal high temperature solar particle receiver. Energy. 29, 687-700.

Bogaerts, W.F., Lampert, C.M., 1983. Materials for photothermal solar-energy conversion. J. Mater. Sci. 18, 2847-2875.

Bohn, M.S., Wang, K.Y., 1988. Experiments and analysis on the molten salt direct absorption receiver concept. J. Sol. Energ.-T. ASME. 110, 45-51.

Bohren, C.F., Huffman, D.R., 1998. Absorption and scattering of light by small particles, Wiley Professional pbk. ed. Wiley-VCH, New York.

Brewster, M.Q., Tien, C.L., 1982. Radiative transfer in packed fluidized beds: dependent versus independent scattering. J. Heat Transf.. 104, 573-579.Caouris, Y., Rigopoulos, R., Tripanagnostopoulos, J., Yianoulis, P., 1978. Novel solar collector. Sol. Energy. 21, 157-160.

Drotning, W.D., 1978. Optical-properties of solar-absorbing oxide particles suspended in a molten-salt heat-transfer fluid. Sol. Energy. 20, 313-319.

Epstein, M., Segal, A., Yogev, A., 1999. A molten salt system with a ground base-integrated solar receiver storage tank. J. Phys. IV France. 09, Pr3-95-Pr93-104.

Fend, T., Pitz-Paal, R., Reutter, O., Bauer, J., Hoffschmidt, B., 2004. Two novel high-porosity materials as volumetric receivers for concentrated solar radiation. Sol. Energ. Mat. Sol. C. 84, 291-304.

Harries, J.E., 2000. Physics of the Earth's radiative energy balance. Contemp. Phys. 41, 309-322.

Healy, J.J., de Groot, J.J., Kestin, J., 1976. The theory of the transient hot-wire method for measuring thermal conductivity. Physica B+C. 82, 392.

Hunt, A.J., 1978. Small particle heat exhangers. Lawrence Berkeley Laboratory.

Kumar, S., Tien, C.L., 1990. Analysis of combined radiation and convection in a particulate-laden liquid-film. J. Sol. Energ.-T. ASME. 112, 293-300.

Kribus, A., Zaibel, R., Carey, D., Segal, A., Karni, J., 1998. A solar-driven combined cycle power plant. Sol. Energy. 62, 121.

Langston, L.S., 2009. Efficiency by the Numbers. Mechanical Engineering Magazine (ASME). http://memagazine.asme.org/Web/Efficiency_by_Numbers.cfm

Romero, M., Buck, R., Pacheco, J.E., 2002. An update on solar central receiver systems, projects, and technologies. J. Sol. Energ.-T. ASME. 124, 98-108.

Miller, F.J., Koenigsdorff, R.W., 1991. Theoretical-analysis of a high-temperature small-particle solar receiver. Sol. Energ. Mater. 24, 210-221.

Miller, F.J., Koenigsdorff, R.W., 2000. Thermal modeling of a small-particle solar central receiver. J. Sol. Energ.-T. ASME. 122, 23-29.

Modest, M.F., 2003. Radiative Heat Transfer, Second ed. Academic Press, Burlington.

Moens, L., Blake, D., 2008. Mechanism of Hydrogen Formation in Solar Parabolic Trough Receivers, NREL/TP-510-42468. National Renewable Energy Laboratory, Golden, CO.

Nan, C.W., Birringer, R., Clarke, D.R., Gleiter, H., 1997. Effective thermal conductivity of particulate composites with interfacial thermal resistance. J. Appl. Phys. 81, 6692-6699.

Otanicar, T.P., Phelan, P.E., Golden, J.S., 2009a. Optical properties of liquids for direct absorption solar thermal energy systems. Sol. Energy.

DOI: 10.1016/j.solener.2011.09.029.

Publication source: Solar Energy 86, no. 1, p. 253–265, 2012.

Otanicar, T.P., Phelan, P.E., Prasher, R.S., Rosengarten, G., Taylor, R.A., 2010. Nanofluid-based direct absorption solar collector. J. Renewable Sustainable. 2, 033102.

Otanicar, T.P., Phelan, P.E., Taylor, R.A., Prasher, R.S., 2009b. Impact of size and scattering mode on the optimal solar absorbing nanofluid. San Francisco, California, USA.

Pacheco, J.E., 2001. Demonstration of solar-generated electricity on demand: the solar two project. J. Sol. Energ.-T. ASME. 123, 5-5.

Pitz-Paal, R., Hoffschmidt, B., Böhmer, M., Becker, M., 1997. Experimental and numerical evaluation of the performance and flow stability of different types of open volumetric absorbers under non-homogeneous irradiation. Sol. Energy. 60, 135.

Pitz-Paal, R., Trevor, M.L., Concentrating Solar Power, in: Future Energy, Elsevier, Oxford, 2008, pp. 171.

Sani, E., Barison, S., Pagura, C., Mercatelli, L., Sansoni, P., Fontani, D., Jafrancesco, D., Francini, F., 2010. Carbon nanohorns-based nanofluids as direct sunlight absorbers. Opt. Express. 18, 5179-5187.

Singh, N., Kaushik, S.C., Misra, R.D., 2000. Exergetic analysis of a solar thermal power system. Renew. Energ. 19, 135.

Slocum, A.H., Codd, D.S., Buongiorno, J., Forsberg, C., McKrell, T., Nave, J.-C., Papanicolas, C.N., Ghobeity, A., Noone, C.J., Passerini, S., Rojas, F., Mitsos, A., 2011. Concentrated solar power on demand. Sol. Energy. 85, 1519-1529.

Tyagi, H., Phelan, P., Prasher, R., 2009. Predicted efficiency of a low-temperature nanofluid-based direct absorption solar collector. J. Sol. Energ.-T. ASME. 131.

Webb, B.W., Viskanta, R., 1985. Analysis of heat transfer and solar radiation absorption in an irradiated thin, falling molten salt film. J. Sol. Energ.-T. ASME. 107, 113-119.

Wijeysundera, N.E., Thevendran, V., 1988. A two-dimensional heat transfer analysis of the thermal-trap collector. Sol. Energy. 40, 127.

Yogev, A., Kribus, A., Epstein, M., Kogan, A., 1998. Solar "tower reflector" systems: A new approach for high-temperature solar plants. Int. J. Hydrog. Energy. 23, 239-245.